Cooling times in femtosecond pump-probe experiments of phase transitions with latent heat

Daniel Kazenwadel,[1] Noel Neathery,[1] Saurav Prakash,[2] Ariando Ariando,[2] and Peter Baum[1,*]

[1]*Fachbereich Physik, Universität Konstanz, 78464 Konstanz, Germany*

[2]*Department of Physics, National University of Singapore, 117542 Singapore, Singapore*

(Received 26 July 2023; accepted 19 September 2023; published 23 October 2023)

Ultrafast pump-probe experiments can reveal the physics of complex materials by triggering a reaction with short laser pulses and then looking for the response. However, the repetition rate in such experiments is limited because the sample needs to cool down back to the initial state between subsequent laser excitations. Here we investigate by theory and experiment how this cooling rate depends on the shape and dimensionality of the material. Using VO_2 as the example, a strongly correlated material with an ultrafast phase transition with large latent heat, we report more than six orders of magnitude of change between the cooling times of freestanding thin films, thin films on a substrate, and bulk materials. A numerical latent-heat model reproduces all results and can therefore be generally used to predict the speed of the back reaction in almost all kinds of phase-change materials.

DOI: 10.1103/PhysRevResearch.5.043077

I. INTRODUCTION

In femtosecond pump-probe experiments, a material is investigated by impulsively distorting its properties with a femtosecond laser pulse while the subsequent evolution is observed in the spectral, structural, or magnetic domain by, for example, laser pulses, electron diffraction, or x-ray techniques. On the one hand, researchers want to trigger the pump-probe cycle as rapidly as possible, but on the other hand, the sample needs enough time to return to its ground state and base temperature between subsequent laser excitations. Unless the sample can be replenished, for example, in a liquid or gas jet, the driving laser's repetition rate must be matched to the expected back-reaction dynamics of the investigated materials. In particular, probing techniques that require vacuum or ultrathin materials, for example, ultrafast electron diffraction or attosecond spectroscopy, suffer from a substantial slowness of heat removal away from the laser-excited region into some kind of sample holder or the surrounding medium. The problem becomes even more complicated when a phase transition is involved because the latent heat needs to be deposited and removed each time.

Here we investigate by theory and experiment the back-reaction times of a prototypical complex material of modern condensed-matter research—namely, VO_2—a strongly correlated material with a first-order phase transition from monoclinic/insulator to rutile/metallic at a temperature of $T_{\mathrm{trans}} \approx 68^\circ$ C. There, the crystal structure changes from a monoclinic $P2_1/c$ to a tetragonal $P4_2/mnm$ structure, and resistivity decreases by more than three orders of magnitude [1,2]. Accordingly, there are strong changes in midinfrared reflectivity and transparency [3]. This phase transition enables many technological applications, for example, ultrafast photoelectric switches [4,5], thermochromic windows [6–8], and ultrasensitive bolometers [9]. The transition is of great interest to theoretical physics as well [10–12] because of the strongly correlated nature of the material and high electron-phonon coupling [13].

The phase transition can be triggered by various means, for example, by classical thermal heating above the transition temperature [1], ultrafast laser pulses [14], terahertz radiation [15], strain [16], as well as strong electric fields [17]. The dynamics of the phase transition after ultrafast laser excitation is typically probed by ultrashort laser pulses [18,19], terahertz radiation [20], electrons [21–23], or x-rays from free-electron lasers [24,25]. While the transition from the insulating/low-temperature phase to the metallic/high-temperature phase can occur within tens to hundreds of femtoseconds [20–28], the speed of the back transition is limited by the huge latent heat of $L = 51.8$ kJ/kg [29], equivalent to the energy needed to heat the sample by 70 K, which needs to be transported away after each laser excitation before repeating the experiment.

II. SAMPLE PREPARATION AND MEASUREMENT SETUP

In our experiments, we investigate four different experimental geometries with different dimensionality: a macroscopic single crystal, a freestanding thin film in air, a freestanding thin film in vacuum, and a thin film on a bulk substrate. The bulk single crystals are grown via thermal decomposition of V_2O_5 at 975° C under an argon atmosphere at a growth speed limited by liquid-phase diffusion [2]. The as-grown surfaces have $>1\,\mathrm{mm}^2$ in area and are optically flat [2]. Thin films of VO_2 have been grown on a 0.5-mm thick,

*peter.baum@uni-konstanz.de

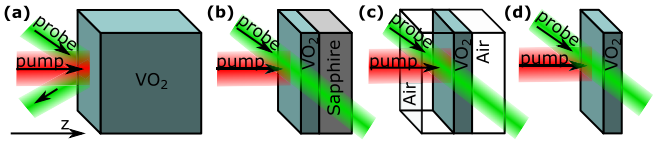

FIG. 1. Investigated sample geometries and measurement schemes. (a) Bulk single crystal (blue) measured in reflectivity. The pump beam (red) hits the sample orthogonally and the probe beam (green) measures the induced reflectivity change. (b) Thin film/layer of VO_2 on a sapphire substrate (gray; substrate thickness not to scale). (c) Freestanding thin film in air (white). (d) Freestanding thin film in a vacuum. All the thin films are measured in transmission with the photodiode placed behind the materials.

c-cut sapphire single-crystalline substrate using pulsed laser deposition [30]. The resulting VO_2 films are 60 nm thick, with the VO_2 (020) plane of the monoclinic phase parallel to Al_2O_3 (0006) [31]. For the production of freestanding thin films, we use a sacrificial $Sr_3Al_2O_6$ layer between sapphire and VO_2 that is later dissolved in H_2O [32]. The resulting flakes with a thickness of 50 nm are then scooped up from the water surface onto a transmission electron microscopy grid (50-μm mesh).

Figure 1 depicts the experimental geometry of our femtosecond pump-probe experiments. The pump pulses (red) are obtained from a femtosecond laser (Pharos, Light Conversion) at a center wavelength of 1030 nm, a pulse duration of 300 fs, and a repetition rate of 1 to 200 kHz. These pulses are focused onto our four types of samples (blue) under normal incidence. As a probe (green), we use an infrared continuous-wave laser in combination with an ultrafast infrared photodiode and a GHz oscilloscope. The focal size of the femtosecond pump beam (full width at half maximum of 140 μm) is about twice as large as the focal diameter of the probe beam. The continuous-wave laser (AP-Tm-392 & AP-AMP-40, AdValuePhotonics) has a wavelength of 2 μm and hits the samples at an angle of incidence of $\alpha \approx 45^\circ$. The reflection or transmission from the sample surface is then collimated and focused onto an ultrafast InGaAs photodiode with a rise time of 2 ns (G12182-003K, Hamamatsu). The diode output is amplified with a transimpedance amplifier (HCA-400M-5K-C, Femto) at a rise time of ∼1 ns, and then analyzed with a sampling oscilloscope (WaveSurfer 44MXs-B, LeCroy). The bulk material is measured in reflection [see Fig. 1(a)], and the thin-film samples are measured in transmission [see Figs. 1(b)–1(d)].

III. NUMERICAL SIMULATION

We simulate the dynamical evolution $\partial T/\partial t$ of our sample's temperature $T(z,t)$ in space and time using the second-order differential equation for heat conductivity,

$$\frac{\partial \boldsymbol{T}}{\partial \boldsymbol{t}} = \frac{\partial^2 \boldsymbol{T}}{\partial^2 \boldsymbol{z}} \frac{\boldsymbol{\kappa}}{\boldsymbol{\rho c_p(T)}}, \tag{1}$$

with the heat conductivity $\kappa = 9$ W/mK [33], the density $\rho = 4.6\,\mathrm{g/cm^3}$ [34], and the temperature-dependent heat capacity $c_p(T)$. For the high-temperature ($T > T_{\mathrm{trans}}$) and low-temperature ($T < T_{\mathrm{trans}}$) phases, we use the measured heat capacities $c_{\mathrm{low}} = 656$ J/kg K and $c_{\mathrm{high}} = 780$ J/kg K [34]. If there is latent heat, there is a discontinuity in the heat capacity that impairs the differentiability of Eq. (1). We therefore introduce a finite width $w_{\mathrm{trans}} = 0.1$ K of the phase transition slopes, motivated by the finite measured slopes in experiments [2] and phase coexistence during the transition [35,36] that are caused by slight inhomogeneities and defects of the materials [36,37]. Consequently, the latent heat of $L = 51.8$ kJ/kg [29] is distributed around $T_{\mathrm{trans}} = 338$ K at a width of $w_{\mathrm{trans}} = 0.1$ K according to

$$c_p(T) = \frac{2 \cdot L}{w_{\mathrm{trans}}} \sin^2\left(\frac{(T - T_{\mathrm{trans}}) \cdot \pi}{w_{\mathrm{trans}}}\right) + c_{\mathrm{low}} + (c_{\mathrm{high}} - c_{\mathrm{low}}) \cdot \sin^2\left(\frac{(T - T_{\mathrm{trans}}) \cdot \pi}{2 \cdot w_{\mathrm{trans}}}\right), \tag{2}$$

where the $\sin^2$ terms for the shape of the transition are chosen to provide a nicely differentiable form. Using the values of the latent heat and heat capacity just estimated, we see that the latent heat amounts to the same energy needed to heat the sample by more than 70 K. Therefore, ignoring latent heat [18] leads to substantial offsets in recorded temperatures as well as incorrect timescales due to increased temperature gradients. Figure 2(a) shows this c_p as a function of T (solid line) together with a typical depth-dependent temperature profile $T(z)$ (dashed line) after one laser excitation pulse.

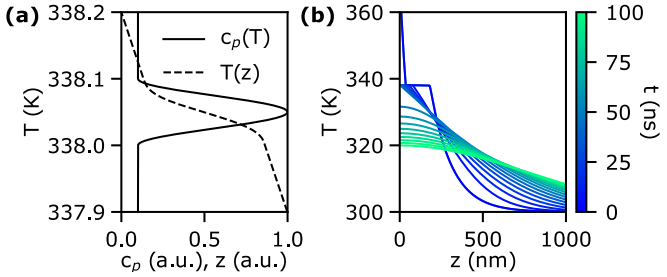

FIG. 2. Heat capacity and simulated temperature profiles. (a) Dependence of heat capacity $c_p(T)$ on temperature (solid line) and initial temperature profile $T(z)$ in the sample after one excitation laser pulse (dashed line). The direction z is orthogonal to the sample surface and parallel to the pump beam direction (see Fig. 1). (b) Simulated time-dependent temperature profiles in the bulk sample after laser excitation. Colors denote the time delay after laser excitation at $t = 0$ ns.

To simulate the quasi-instantaneous heating by the femtosecond laser source, the heat capacity is integrated into an energy $E(T)$ that is required to heat the sample from room temperature ($T_0 = 300$ K) up to a laser-induced temperature T according to $E(T) = \int_{T_0}^{T} c_p(T)$. By taking the inverse of this function, $T(E)$, and assuming an exponential decay of the deposited laser pump fluence F (up to $10\,\mathrm{mJ/cm^2}$ in the experiments) into an optical penetration depth of $\delta_{\mathrm{pump}} = 130$ nm in VO_2 [38], we obtain the initial temperature profile $T(z, F) = T\,(\exp(-z/\delta_{\mathrm{pump}}) \cdot F/\delta_{\mathrm{pump}})$ directly after the laser excitation. The dashed line in Fig. 2(a) shows the result. The peak of the heat capacity around the transition temperature results in a decrease of deposited temperature in an almost steplike but still differentiable shape.

We simulate the subsequent time evolution of this temperature profile with a one-dimensional finite-element approach. Thermally isolating boundaries are applied to both ends of

the simulated length. For each time step and simulation cell, the second derivative of the temperature is calculated and converted into a temperature change according to Eq. (1). A time step of ∼100 fs is sufficient for converging results.

Figure 2(b) shows a typical series of heat profiles for the case of a bulk material as a function of time after laser excitation. The initial temperature profile just after laser excitation (blue) shows an exponential decrease at the sample surface ($z = 0$ nm), then a constant temperature plateau, and finally an exponential decrease again. Close to the sample surface, all of the material is far above the transition temperature, and latent heat effects are negligible. In the plateau, the material is partially transformed in proportion to the deposited excitation energy density, resulting in an almost constant temperature profile. Deeper inside, the entire material is below T_{trans}, and the temperature becomes exponential again. As time proceeds (blue to green), heat gets transported deeper into the sample. The high temperature at the surface is quickly diminished as the dispersing heat transforms more of the material. At the same time, the plateau becomes smaller from the inside, because heat is removed into the cold material. On longer timescales ($t > 50$ ns), the material is completely transformed back, and the subsequent temperature profile slowly equilibrates toward a uniform temperature profile (green).

To simulate the thin-film samples on sapphire substrates, we use a heat conductivity $\kappa_S = 30$ W/mK, heat capacity $c_{p,S} = 764$ J/kg K, and density $\rho_S = 398$ g/cm^3 for sapphire [39]. The thermal conductivity at the interface is assumed to be the average of the two materials' thermal conductivities because the epitaxial growth does not produce too many dislocations or other crystal faults, so surface-specific heat transport effects are not substantial. When simulating freestanding thin films in air, we use estimated values for heat capacity and thermal conductivity of air in order to account for convection effects (see Appendix). We assume that most heat is still transported in the z direction (into the air). This effect is dominant, because the timescales of the cooling changes by one order of magnitude when going from an air environment into the vacuum [27].

In the freestanding thin film in a vacuum, we need to invoke heat conductivity in a radial direction according to $\frac{\partial T}{\partial t} = (\frac{\partial^2 T}{\partial^2 r} + \frac{\partial T}{\partial r} \cdot \frac{1}{r}) \frac{\kappa}{\rho c_p(T)}$. We ignore effects in the z direction [40] because the 60-nm-thick film homogenizes within <10 ns (see Appendix). The resulting temperature profiles are now based on the Gaussian laser spot instead of the exponential decay induced by the limited laser penetration depth.

In order to simulate the influence of our resulting temperature profiles on the measured quantity in pump-probe spectroscopy, that is, the changes of reflection or transmission of our probe pulses due to the phase transition, we calculate for each material and each time step the relative amount of simulation cells that are in the high-temperature phase ($T > T_{\text{trans}}$) and then use this quantity to calculate the reflectivity or transmission of the probe. Cells that are in the transition interval $T_{\text{trans}} - w_{\text{trans}} < T < T_{\text{trans}}$ [in the plateau of Fig. 2(b)] are weighted by how far they are along the $c_p(T)$ curve of Fig. 2(a). To simulate the finite penetration depth of our probe laser, it would be ideal to weight each simulation cell exponentially with the local intensity of the probe beam, but since this procedure is found not to alter the results significantly, it was omitted for simplicity. The resulting simulated time-dependent reflectivity is then convoluted with the photodiode's rise time of $\sigma = 2.05$ ns to obtain traces comparable to our measurement results.

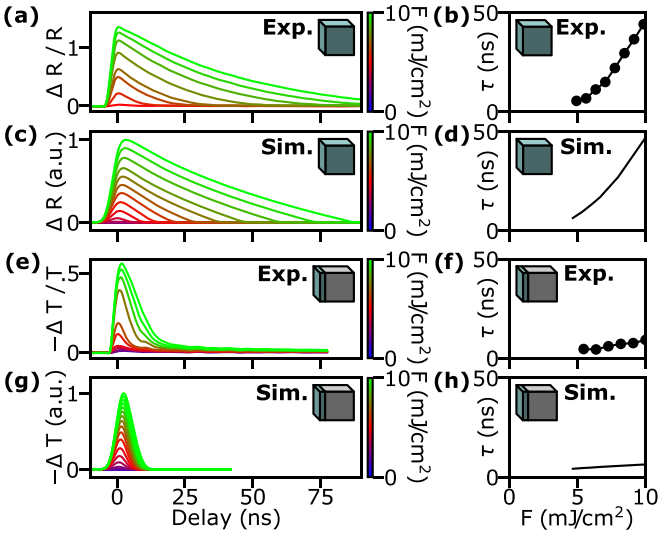

FIG. 3. Cooling dynamics in bulk samples. (a) Measured time-dependent reflectivity of the bulk material for different pump fluences (colors from blue to green). (b) Time constant τ of the cooling process as a function of excitation fluence. (c) Simulated time-dependent reflectivity of the bulk material. (d) Simulated time constant of the cooling process of the bulk material. (e) Measured time-dependent transmittivity of the VO_2 thin film on a bulk sapphire substrate. The slight bump at approximately 10 ns is caused by an impedance mismatch in the detection. (f) Measured time constant of the thin film on a substrate. (g) Simulated time-dependent transmittivity of the thin film on a substrate. (h) Simulated time constant of the cooling process of the thin film on a substrate.

IV. MEASUREMENTS AND SIMULATION RESULTS

We now report the results of pump-probe measurements of the bulk samples and thin films on bulk substrates after femtosecond laser excitation in comparison to the simulations. Figure 3 shows a summary of these results. In Fig. 3(a), we plot the measured time-dependent reflectivity traces of the macroscopic bulk sample as a function of excitation fluence. The corresponding measured time constants are plotted in Fig. 3(b). For comparison, Fig. 3(c) shows the result of our simulations, and Fig. 3(d) shows the simulated time constants. Figure 3(e) shows the measurement of our thin films on a sapphire substrate, and Fig. 3(f) shows the measured time constants. For comparison, Fig. 3(g) shows our simulation results, and Fig. 3(h) reports the simulated decay times.

In all data sets, we see a quick rise of the reflectivity or decrease in transmittivity by several tens of percent, followed by a decay on slower timescales. For fluences below about 5 mJ/cm^2, no change in reflectivity can be observed because the material does not reach the transition temperature of 340 K. Above the fluence threshold, the level of the initial rise increases because more and more material is transformed. At low fluences, the measured rise time of the primary part of the dynamics fits the rise time of our photodiode of $\sigma = 2.05$ ns.

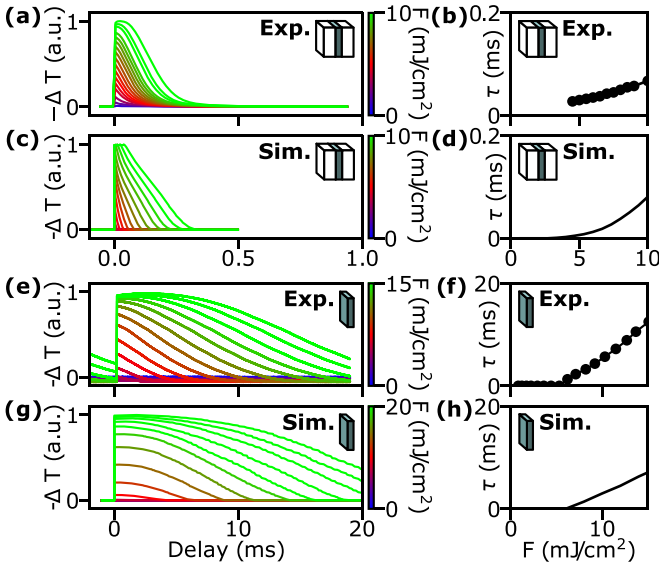

FIG. 4. Cooling dynamics in freestanding thin films. (a) Measured time-dependent transmittivity of the thin-film sample in air for different pump fluences (colors from blue to green). (b) Time constant τ of the cooling process as a function of excitation fluence. (c) Simulated time-dependent transmittivity of the thin-film sample in air. (d) Simulated time constant of the cooling process of the thin-film sample in air. (e) Measured time-dependent transmittivity of the VO_2 thin film on a 150-nm-thick silicon nitride substrate in a vacuum (taken from Ref. [27]). (f) Measured time constant of the thin film in a vacuum. (g) Simulated time-dependent transmittivity of the thin film in a vacuum. (h) Simulated time constant of the cooling process of the thin film in a vacuum.

At higher fluences, the rise time is slightly increased. The simulations [compare Figs. 3(a) and 3(b) with Figs. 3(c) and 3(d)] show that this effect is caused by surplus heat from the front of the sample, which is gradually transported to the back, where it pushes previously untransformed material through the transition at a later time.

In both materials (bulk and thin film on a substrate), the back reaction occurs on a nanosecond timescale, and the decay slows down for increasing excitation fluences (color scale) because more and more latent heat needs to be transported away before the front part is cool enough to transform back. The figures in the right column of Fig. 4 show the measured and simulated cooling times τ (decays to 1/e). At fluences below the phase transition threshold ($\sim$5 mJ/cm^2), no material is transformed, and therefore no signal is observed, and no time constant can be calculated. At the threshold power, the cooling time is limited by the time resolution of our setup and then significantly increases for higher excitation fluences. Around the transition temperature (fluences of 5 to 8 mJ/cm^2), experiments show a phase coexistence of metallic and insulating phases [41,42], which in our simulations is covered by a distribution of the latent heat around w_{trans} [see Eq. (2)]. Here, the agreement between measurement and simulations shows that details of the hysteresis and fractal domain patterns on nanometer dimensions [37] are not significant for our results due to the big spatial size of the optical pump and probe beams, but may show up in electron microscopy or x-ray diffraction. At large excitation fluences (>8 mJ/cm^2), the front of the material completely transforms into the high-temperature phase. Accordingly, the cooling time is increased.

In comparison to the bulk material, the thin film on a substrate shows almost identical heating dynamics, but cools down much faster (a few nanoseconds compared to tens of nanoseconds) because the sapphire substrate is initially not excited and does not have a latent heat. The small bump at a delay time of approximately 10 ns is caused in the measurements by an impedance mismatch in the detection scheme and is therefore an artifact. The simulation [see Figs. 3(g) and 3(h)] assumes a perfect thermal contact between VO_2 and the sapphire without interface effects, and the results are therefore slightly faster than the experiment.

The dynamics change substantially when going from bulk materials or bulk substrates to a situation where the material is a freestanding membrane without support. Such a geometry is required, for example, in ultrafast electron diffraction or attosecond extreme ultraviolet spectroscopy due to the limited penetration depths of those measurement techniques. Figure 4 shows the results that we obtain from a freestanding thin film in a vacuum or air. Figure 4(a) shows the measured time-dependent reflectivity traces of a VO_2 membrane (blue) in air (white). The measured cooling times are plotted in Fig. 4(b). For comparison, Fig. 4(c) shows the results of our simulation, and Fig. 4(d) shows the simulated time constants. Figure 4(e) shows measurement results on thin films in a vacuum (taken from Ref. [27]), and Fig. 4(f) shows the evaluated time constants. For comparison, Fig. 4(g) shows the results of our simulations, including radial heat conduction, and Fig. 4(h) reports the simulated time constants.

As before, we see in all data traces a fast rise followed by a much slower decay. However, the timescale of the decay is now in the millisecond range, several orders of magnitude slower than before. The reason is that heat now has to be removed inefficiently into the air [Fig. 4(d)] or radially across the whole spot size [Figs. 4(e)–4(h)] instead of an efficient removal into a cold bulk substrate in the z direction. Again, the measured and simulated cooling time becomes longer for increased laser fluences, because more and more total energy needs to be removed. At the highest excitation fluences, the curves show saturation—that is, the signal strength at early times does not increase with fluence anymore in a proportional way. Eventually, the material within the probed volume is completely transformed and additional energy can only produce higher temperatures, but not more high-temperature material—the quantity that affects the transmittivity.

In the freestanding thin-film samples in air, two regimes can be observed. At lower fluences (5 to 7 mJ/cm^2), we see a single exponential behavior with decay times around 0.1 ms. In this regime, heat removal into the air, although much less efficient than into a substrate, is dominant over radial heat conductivity into the sample holder. Above 7 mJ/cm^2, the measured and simulated time traces become nonexponential and reveal substantially higher decay times. We attribute these observations to the formation of a gradient of hot air around the two sample surfaces that is impeding and slowing down the heat removal.

In the freestanding thin-film samples in a vacuum, the measurements and simulations [Figs. 4(e)–4(h)] reveal an

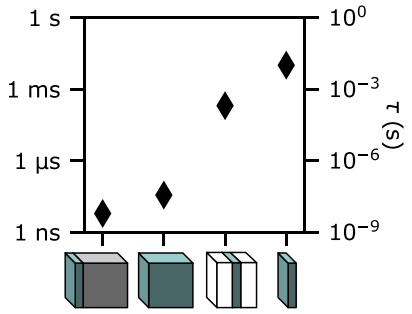

FIG. 5. Back-reaction times. Diamonds show the typical measured cooling times in (from left to right) a VO_2 layer (blue) on a sapphire substrate (gray), a bulk crystal (blue), a freestanding membrane (blue) in air (white), and a freestanding membrane (blue) in a vacuum. The cooling speed changes by more than six orders of magnitude depending on the sample geometry.

even longer cooling time of tens of milliseconds. Also, the curves are nonexponential and more roundish for almost all excitation fluences (e.g., red curves). These two observations show that radial heat removal is now the only mechanism at work. No heat can be transported away from the surfaces (z direction), and heat removal can only proceed radially within the film, resulting in a first-order term in the heat conductivity equation (presented earlier). The measured and simulated time constants for the cooling process increase with laser fluence, because the latent heat of more and more converted material needs to be removed, at a close to constant temperature gradient. There is a small discrepancy between measured and calculated timescales of about 1.5, which we attribute to the onset of multipulse heat accumulation and an increase of base temperature in the experiment, although the repetition rate is only 50 Hz [27].

Figure 5 shows an overview of all measured cooling times in the four experimental geometries in this work. Between a VO_2 layer coated on a sapphire substrate, a bulk single crystal, a freestanding membrane in air, and a freestanding membrane in a vacuum, we see a total of six orders of magnitude of change from nanoseconds to milliseconds in the cooling time.

V. CONCLUSION

The combined results show how the geometry and surroundings of a material with latent heat substantially influence the dynamics of the back transformation and therefore limit the maximum pump-probe repetition rate that can be applied in ultrafast experiments. While bulk crystals and thin films on a substrate allow laser repetition rates in the MHz regime, freestanding thin films in a vacuum and air require repetition rates in the Hertz regime. The reason for this extreme dependency is the latent heat. It is difficult to remove because it strongly decreases the temperature gradients in the sample by breaking the linear dependence of absorbed fluence and temperature [see Fig. 2(a)], resulting in a slower cooling process. For ultrafast electron diffraction experiments, which often require ultrathin samples in a vacuum, our results show that, without using further cooling mechanisms, only repetition rates in the regime of hundreds of Hertz can be applied.

Furthermore, our simulations show how inhomogeneously typical samples are excited in a pump-probe experiment, in which a limited penetration depth of the excitation laser [see Fig. 2(b)] results in only partial transformation of the samples. It is therefore not enough to make the pump spots bigger than the probe spots, but the two penetration depths need to be adapted and taken into account as well, in addition to choosing an optimum frequency of pump and probe. Fortunately, our reported numerical model for heat conduction with latent heat can account for almost all such effects—in particular, the influences of depth-dependent excitations, diverging heat capacities, and out-of-plane and in-plane heat conductivity for almost any solid-state material. The quantitative agreement of our simulations with all experiments shows the predictive capabilities of our approach, providing researchers with a tool for designing their pump-probe experiment for optimum performance and validity.

ACKNOWLEDGMENTS

The authors acknowledge financial support by evangelisches Studienwerk e.V. and Sonderforschungsbereich SFB1432. The work by S.P. and A.A. was supported by the Science and Engineering Research Council of A*STAR (Agency for Science, Technology and Research) Singapore (Grant No. M22L1b0110). They thank J. Holder for helpful discussions and S. Wall for raw data from Ref. [27].

APPENDIX: DETAILS OF THE SIMULATIONS

To simulate the cooling effect of air on our thin-film sample in the presence of convection, we use an effective heat conductivity of 0.03 W/mK and a heat capacity of 1870 J/kg K. These values lead to matching results to the data [Fig. 4(a)] and show similar scaling behavior as observed in the experiments. Transport in the radial direction is ignored, because air cooling is the dominant effect [27]. To simulate the VO_2 films in a vacuum, several peculiarities of the experiment described by Vidas *et al.* [27,28] have to be accounted for. The pump spot was assumed to be circular, with a diameter of 340 µm. Other than in our own thin-film measurements, Vidas *et al.* [27,28] did not use completely freestanding thin films, but grew their 70-nm-thick films on a 150-nm thin Si_3N_4 substrate. Since the length scales in the z direction are still three orders of magnitude smaller than the radial scales, and the material parameters of Si_3N_4 and VO_2 are quite similar besides the latent heat, which is zero in Si_3N_4, we can assume a homogeneous temperature along z. This allows us to use an effective medium approach where we weigh the materials' parameters of VO_2 and Si_3N_4 accordingly and use an effective medium with these values in our simulations. The remaining differences in recorded and simulated timescales are caused by the significant heat accumulation observed by Vidas *et al.* [27,28] in their experiments, which we did not take into account for the sake of simplicity.

[1] F. J. Morin, Oxides which show a metal-to-insulator transition at the Neel temperature, Phys. Rev. Lett. **3**, 34 (1959).

[2] N. Sprinkart, D. Kazenwadel, R. Hartmann, and P. Baum, Liquid-diffusion-limited growth of vanadium dioxide single crystals, Phys. Rev. Res. **5**, 013028 (2023).

[3] J. A. Ramirez-Rincon, C. L. Gomez-Heredia, A. Corvisier, J. Ordonez-Miranda, T. Girardeau, F. Paumier, C. Champeaux, F. Dumas-Bouchiat, Y. Ezzahri, K. Joulain, O. Ares, and J. J. Alvarado-Gil, Thermal hysteresis measurement of the VO_2 dielectric function for its metal-insulator transition by visible-IR ellipsometry, J. Appl. Phys. **124**, 195102 (2018).

[4] C. Lu, Q. Lu, M. Gao, and Y. Lin, Dynamic manipulation of THz waves enabled by phase-transition VO_2 thin film, Nanomaterials **11**, 114 (2021).

[5] T. Kang, Z. Ma, J. Qin, Z. Peng, W. Yang, T. Huang, S. Xian, S. Xia, W. Yan, Y. Yang, Z. Sheng, J. Shen, C. Li, L. Deng, and L. Bi, Large-scale, power-efficient Au/VO_2 active metasurfaces for ultrafast optical modulation, Nanophotonics **10**, 909 (2020).

[6] Y. Cui, Y. Ke, C. Liu, Z. Chen, N. Wang, L. Zhang, Y. Zhou, S. Wang, Y. Gao, and Y. Long, Thermochromic VO_2 for energy-efficient smart windows, Joule **2**, 1707 (2018).

[7] S. Wang, T. Jiang, Y. Meng, R. Yang, G. Tan, and Y. Long, Scalable thermochromic smart windows with passive radiative cooling regulation, Science **374**, 1501 (2021).

[8] K. Tang, K. Dong, J. Li, M. P. Gordon, F. G. Reichertz, H. Kim, Y. Rho, Q. Wang, C.-Y. Lin, C. P. Grigoropoulos, A. Javey, J. J. Urban, J. Yao, R. Levinson, and J. Wu, Temperature-adaptive radiative coating for all-season household thermal regulation, Science **374**, 1504 (2021).

[9] C. Chen, X. Yi, X. Zhao, and B. Xiong, Characterizations of VO_2-based uncooled microbolometer linear array, Sens. Actuator A: Phys. **90**, 212 (2001).

[10] A. S. Belozerov, M. A. Korotin, V. I. Anisimov, and A. I. Poteryaev, Monoclinic M1 phase of VO_2: mott-hubbard versus band insulator, Phys. Rev. B **85**, 045109 (2012).

[11] F. Grandi, A. Amaricci, and M. Fabrizio, Unraveling the Mott-Peierls intrigue in vanadium dioxide, Phys. Rev. Res. **2**, 013298 (2020).

[12] O. Nájera, M. Civelli, V. Dobrosavljevic, and M. J. Rozenberg, Resolving the VO_2 controversy: Mott mechanism dominates the insulator-to-metal transition, Phys. Rev. B **95**, 035113 (2017).

[13] K. Okazaki, S. Sugai, Y. Muraoka, and Z. Hiroi, Role of electron-electron and electron-phonon interaction effects in the optical conductivity of VO_2, Phys. Rev. B **73**, 165116 (2006).

[14] D. Wegkamp and J. Stähler, Ultrafast dynamics during the photoinduced phase transition in VO_2, Prog. Surf. Sci. **90**, 464 (2015).

[15] A. X. Gray *et al.*, Ultrafast terahertz field control of electronic and structural interactions in vanadium dioxide, Phys. Rev. B **98**, 045104 (2018).

[16] J. H. Park, J. M. Coy, T. S. Kasirga, C. Huang, Z. Fei, S. Hunter, and D. H. Cobden, Measurement of a solid-state triple point at the metal-insulator transition in VO_2, Nature (London) **500**, 431 (2013).

[17] B. Wu, A. Zimmers, H. Aubin, R. Ghosh, Y. Liu, and R. Lopez, Electric-field-driven phase transition in vanadium dioxide, Phys. Rev. B **84**, 241410(R) (2011).

[18] M. F. Jager, C. Ott, P. M. Kraus, C. J. Kaplan, W. Pouse, R. E. Marvel, R. F. Haglund, D. M. Neumark, and S. R. Leone, Tracking the insulator-to-metal phase transition in VO_2 with few-femtosecond extreme UV transient absorption spectroscopy, Proc. Natl. Acad. Sci. USA **114**, 9558 (2017).

[19] D. Wegkamp, M. Herzog, L. Xian, M. Gatti, P. Cudazzo, C. L. McGahan, R. E. Marvel, R. F. Haglund, A. Rubio, M. Wolf, and J. Stähler, Instantaneous band gap collapse in photoexcited monoclinic VO_2 due to photocarrier doping, Phys. Rev. Lett. **113**, 216401 (2014).

[20] A. Pashkin, C. Kübler, H. Ehrke, R. Lopez, A. Halabica, R. F. Haglund, R. Huber, and A. Leitenstorfer, Ultrafast insulator-metal phase transition in VO_2 studied by multiterahertz spectroscopy, Phys. Rev. B **83**, 195120 (2011).

[21] P. Baum, D. S. Yang, and A. H. Zewail, 4D Visualization of transitional structures in phase transformations by electron diffraction, Science **318**, 788 (2007).

[22] D. S. Yang, P. Baum, and A. H. Zewail, Ultrafast electron crystallography of the cooperative reaction path in vanadium dioxide, Struct. Dynam. **3**, 034304 (2016).

[23] V. R. Morrison, R. P. Chatelain, K. L. Tiwari, A. Hendaoui, A. Bruhács, M. Chaker, and B. J. Siwick, A photoinduced metal-like phase of monoclinic VO_2 revealed by ultrafast electron diffraction, Science **346**, 445 (2014).

[24] S. Wall, S. Yang, L. Vidas, M. Chollet, J. M. Glownia, M. Kozina, T. Katayama, T. Henighan, M. Jiang, T. A. Miller, D. A. Reis, L. A. Boatner, O. Delaire, and M. Trigo, Ultrafast disordering of vanadium dimers in photoexcited VO_2, Science **362**, 572 (2018).

[25] A. S. Johnson, D. Perez-Salinas, K. M. Siddiqui, S. Kim, S. Choi, K. Volckaert, P. E. Majchrzak, S. Ulstrup, N. Agarwal, K. Hallman *et al.*, Ultrafast x-ray imaging of the light-induced phase transition in VO_2, Nat. Phys. **19**, 215 (2023).

[26] A. Cavalleri, C. Tóth, C. W. Siders, J. A. Squier, F. Ráksi, P. Forget, and J. C. Kieffer, Femtosecond structural dynamics in VO_2 during an ultrafast solid-solid phase transition, Phys. Rev. Lett. **87**, 237401 (2001).

[27] L. Vidas, D. Schick, E. Martinez, D. Perez-Salinas, A. Ramos-Álvarez, S. Cichy, S. Batlle-Porro, A. S. Johnson, K. A. Hallman, R. F. Haglund, and S. Wall, Does VO_2 host a transient monoclinic metallic phase? Phys. Rev. X **10**, 031047 (2020).

[28] L. Vidas, The insulator-metal phase transition in VO_2 measured at nanometer length scales and femtosecond time scales, Ph.D. dissertation, Universitat Politècnica de Catalunya, Institut de Ciències Fotòniques, 2019, doi: 10.5821/dissertation-2117-134615.

[29] C. N. Berglund and H. J. Guggenheim, Electronic properties of VO_2 near the semiconductor-metal transition, Phys. Rev. **185**, 1022 (1969).

[30] A. Srivastava, H. Rotella, S. Saha, B. Pal, G. Kalon, S. Mathew, M. Motapothula, M. Dykas, P. Yang, E. Okunishi, D. D. Sarma, and T. Venkatesan, Selective growth of single phase VO_2 (*a*, *b*, and *m*) polymorph thin films, APL Mater. **3**, 026101 (2015).

[31] Y. Zhao, J. H. Lee, Y. Zhu, M. Nazari, C. Chen, H. Wang, A. Bernussi, M. Holtz, and Z. Fan, Structural, electrical, and terahertz transmission properties of VO_2 thin films grown on *c*-, *r*-, and *m*-plane sapphire substrates, J. Appl. Phys. **111**, 053533 (2012).

[32] D. Lu, D. J. Baek, S. S. Hong, L. F. Kourkoutis, Y. Hikita, and H. Y. Hwang, Synthesis of freestanding single-crystal perovskite films and heterostructures by etching of sacrificial water-soluble layers, Nat. Mater. **15**, 1255 (2016).

[33] L. Chen, Z. Xiang, C. Tinsman, T. Asaba, Q. Huang, H. Zhou, and L. Li, Enhancement of thermal conductivity across the metal-insulator transition in vanadium dioxide, Appl. Phys. Lett. **113**, 061902 (2018).

[34] M. Rodriguez-Vega, M. T. Simons, E. Radue, S. Kittiwatanakul, J. Lu, S. A. Wolf, R. A. Lukaszew, I. Novikova, and E. Rossi, Effect of inhomogeneities and substrate on the dynamics of the metal-insulator transition in VO_2 thin films, Phys. Rev. B **92**, 115420 (2015).

[35] A. S. Johnson, J. V. Conesa, L. Vidas, D. Perez-Salinas, C. M. Günther, B. Pfau, K. A. Hallman, R. F. Haglund, S. Eisebitt, and S. Wall, Quantitative hyperspectral coherent diffractive imaging spectroscopy of a solid-state phase transition in vanadium dioxide, Sci. Adv. **7**, eabf1386 (2021).

[36] L. Vidas, C. M. Günther, T. A. Miller, B. Pfau, D. Perez-Salinas, E. Martnez, M. Schneider, E. Gührs, P. Gargiani, M. Valvidares, R. E. Marvel, K. A. Hallman, R. F. Haglund, S. Eisebitt, and S. Wall, Imaging nanometer phase coexistence at defects during the insulator-metal phase transformation in VO_2 thin films by resonant soft x-ray holography, Nano Lett. **18**, 3449 (2018).

[37] J. Holder, D. Kazenwadel, P. Nielaba, and P. Baum, Determination of the nearest-neighbor interaction in VO_2 via fractal dimension analysis, arXiv:2306.09722.

[38] C. Wan, Z. Zhang, D. Woolf, C. M. Hessel, J. Rensberg, J. M. Hensley, Y. Xiao, A. Shahsafi, J. Salman, S. Richter, Y. Sun, M. M. Qazilbash, R. Schmidt-Grund, C. Ronning, S. Ramanathan, and M. A. Kats, On the optical properties of thin-film vanadium dioxide from the visible to the far infrared, Ann. Phys. **531**, 1900188 (2019).

[39] E. R. Dobrovinskaya, L. A. Lytvynov, and V. Pishchik, *Sapphire Material, Manufacturing, Applications* (Springer, London, 2009).

[40] S. R. Tauchert, M. Volkov, D. Ehberger, D. Kazenwadel, M. Evers, H. Lange, A. Donges, A. Book, W. Kreuzpaintner, U. Nowak, and P. Baum, Polarized phonons carry angular momentum in ultrafast demagnetization, Nature (London) **602**, 73 (2022).

[41] M. M. Qazilbash, M. Brehm, B.-G. Chae, P.-C. Ho, G. O. Andreev, B.-J. Kim, S. J. Yun, A. V. Balatsky, M. B. Maple, F. Keilmann, H.-T. Kim, and D. N. Basov, Mott transition in VO_2 revealed by infrared spectroscopy and nano-imaging, Science **318**, 1750 (2007).

[42] A. Sohn, T. Kanki, K. Sakai, H. Tanaka, and D.-W. Kim, Fractal nature of metallic and insulating domain configurations in a VO_2 thin film revealed by Kelvin probe force microscopy, Sci. Rep. **5**, 10417 (2015).